Reconstructing 1D Fe Single-atom Catalytic Structure on 2D Graphene film for High-efficiency Oxygen Reduction Reaction

Guangqi Zhu[1], Yanling Qi[1], Fan Liu[1], Shenqian Ma[2], Guolei Xiang[2], Fengmin Jin[1], Zigeng Liu[3*], Wei Wang[1,4*]*

[1] School of Chemical Engineering and Technology, Tianjin University, Tianjin, 300072, China

[2] School of Chemical Engineering and Technology, Beijing University of Chemical Technology, Beijing, 100029, China

[3] Institut für Energie und Klimaforschung (IEK-9), Forschungszentrum Jülich GmbH, Jülich, 52425, Germany

[4]Key Laboratory of Metal Fuel Cell of Sichuan Province, Sichuan, 618000, China

**These authors are corresponding authors. Zigeng Liu: zigengliu@gmail.com; Wei Wang: wangweipaper@tju.edu.cn*

Abstract: Inferior catalytic efficiency and short-term endurance in oxygen reduction reaction (ORR) of one/zero-dimension (0D/1D) single-atom catalysts (SACs), resulting from the poor intrinsic activity and ill-organized distribution of metal centers, seriously restrict the application of hydrogen-oxygen fuel cells and metal-air batteries. A self-supporting composite membrane, 1D Fe single-atom catalytic structure conjugated 2D monolayer graphene (Fe SAC@G) with well-ordered atomic-Fe coordination configuration, was synthesized through a reconstruction procedure after selectively tailoring precursor α-FePc under low-temperature vapor condition, and exhibited a higher electrochemical efficiency than commercial Pt/C in 0.1 M KOH solution. DFT-D calculation results manifested the intrinsic ORR activity of Fe SAC@G originates from the newly-formed FeN_4-O-FeN_4 bridge structure with high theoretical ORR equilibrium potential. These findings provide new ways for designing high-activity SACs through flexible synthesizing techniques.

1. Introduction

Electrochemical oxygen reduction reaction (ORR) plays an important role in renewable energy conversion systems, such as hydrogen-oxygen fuel cells and metal-air batteries[1]. Conventionally, Pt-group metals (PGMs) with high intrinsic activity have been predominantly used in catalyzing ORR. However, several issues, including high overpotential, rapid degradation, and expensive cost of the PGMs catalysts greatly hinder the large-scale applications of these systems[2]. Thus, numerous work has been searching for electrocatalysts with excellent performances and cost efficiency[3]. Among the candidates, single-atom catalysts (SACs), where numerous atomic-metal sites separated from each other on solid supports, have drawn great attention as the most promising alternatives to precious metals in accelerating ORR[4].

Today, the most efficient SACs for ORR were fabricated by embedding planar-nitrogen-coordinated transition metal ions (M-N_x) into zero/one-dimensional (0D/1D) carbon matrix[5], such as graphene nanosheets[6], carbon nanotubes[7], and nanofibers[8] through high-temperature pyrolyzing process[9]. However, these SACs generally exhibit low surface atomic-metal doping level, poor electron conductivity and short-term structural stability, due to the initiative reunion of metal centers, inferior crystallization capacity, and weak interactions among the M-N_x sites and supports. In addition, the ill-organized distributions and unpredictable coordination variations during the formation of M-N_x sites through pyrolyzing metal, nitrogen and carbon precursors further hinder the optimization of these catalysts. Moreover, high-temperature treatment is economically unattractive, leading to huge energy consumption and high production cost[10]. Therefore, many aspects need to be improved for SACs.

Since large-scale conjugated two-dimensional (2D) networks, such as graphene or MoS_2 thin films, typically exhibit superior electron conductivity and outstanding structural stability but relatively smaller specific surface area compared with 0D/1D nanomaterials[11], a promising strategy to realize high-speed electron conductivity of SAC is to compactly couple 0D/1D atomic-metal structures with 2D substrates[11d, 12]. Phase Vapor Deposition (PVD) technique allows topologically synthesis of these ordered low-dimension structures on large-scale substrates through separating and recombining conjugated organic molecules (used as precursor) at low temperature and under high vacuum[13]. Among M-N_x SACs, Fe-N_4 sites exhibit

comparable ORR performance to commercial Pt catalyst according to the recent experimental and theoretical research[14], thus α-type iron phthalocyanine (denoted as α-FePc, see Figure S1, Supporting Information), with identified Fe^{2+}-N_4 coordination and flexible molecular modification trait[15], was used as the metal organic precursor for the synthesis.

In this work, the as-prepared Fe SAC@G-110, prepared at a growth temperature of 110 ^{o}C, featured 1D nanocolumns anchored on 2D graphene network. The physical characterizations reveal the structure of Fe SAC@G-110 was composed by two kinds of Fe-coordination configurations, Fe-N_4 site and FeN_4-O-FeN_4 bridge site, and the catalyst displayed superior ORR performance and stability compared with commercial Pt/C catalyst in alkaline solution during electrochemical testing. The DFT-D computational results indicate the intrinsic ORR performance of Fe SAC@G-110 originated from the FeN_4-O-FeN_4 bridge site with high theoretical ORR activity. These results provide a new way to design atomic metal configurations and flexible synthesizing techniques for ORR catalysts.

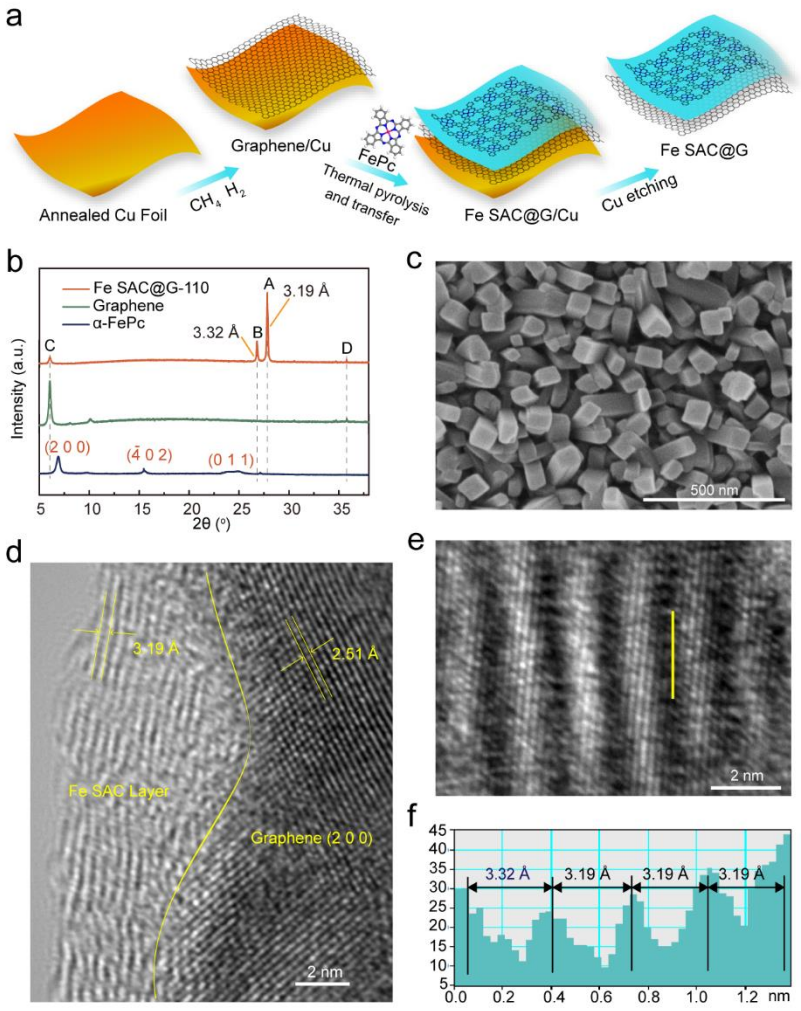

Figure 1. Structural and Morphology analysis of Fe SAC@G-110. a) Schematic illustration for the synthesis route. b) XRD patterns. c) SEM image. d, e) HR-TEM images and f) the corresponding signal curve of the yellow solid line in (e), which manifests two types of interlayer spacing (3.32 Å and 3.19 Å).

2. Results and Discussion

2.1 Structural and Morphology Analysis of Fe SAC@G-110

The synthesis route is schematic illustrated in Figure 1a. Specifically, graphene thin film was first deposited on a piece of annealed copper foil by pyrolyzing CH_4 at 1050 ^oC, denoted as G/Cu (Figure S3, Supporting Information). The precursor α-FePc was then heated at 450 ^oC, at which the Fe-N_4 macrocyclic structure began to decompose (Figure S2, Supporting Information), and transferred to the 110 ^oC region by nitrogen to grow Fe SAC layers on G/Cu substrate (denoted as Fe SAC@G/Cu-110). After etching away the copper layer, the Fe SAC@G-110 composite film is ready for different applications and further investigations (Figure S4 and S5, Supporting Information).

Compared with the precursor and substrate (α-FePc and graphene, respectively), the XRD pattern of Fe SAC@G-110 sample (Figure 1b) shows a pair of adjacent narrow peaks (A and B) positioned at 27º and 28º, indicating a different crystalline structure of Fe SACs@G-110, which will be explored in the following section. SEM image (Figure 1c) of Fe SAC@G-110 displays an ordered column-like morphology with inerratic rectangular profiles (~ 30 nm side length). TEM image (Figure S6, Supporting Information) of an individual nanocolumn exhibits the height of the column of ~80 nm and the corresponding selected area electron diffraction (SEAD) pattern shows bright spots positioned at the reciprocal lattice point of 3.19 Å, manifesting excellent crystal features that in consistent with the XRD results. Furthermore, the high-resolution TEM (HR-TEM) image of the 1D nanocolumns displays uniform stratiform structure, topologically stacked on the (0 0 2) plane of the graphene substrate (Figure 1d). Of note, both the interlayer spacing of 3.32 Å and 3.19 Å were detected from the stacked structure, resulting in a staggered-layer configuration (Figure 1e, f). The high-angle annular dark field - scanning TEM (HAADF-STEM) image and the corresponding EDS elemental mapping (Figure S7, Supporting Information) demonstrate the uniform dispersion of Fe, N and C element in the nanocolumns.

To track the growth procedure of the stratiform structure, SEM images were taken for the Fe SAC@G-110 catalysts prepared for a range of growth period from 5 s to 60 min (Figure S8, Supporting Information). The results suggest that the growth of the 1D nanocolumns first proceeded a quick nucleation and subsequent growth, in a mutual independent way, along the smooth surface of graphene film until completely covering the surface, then followed by a new nucleation procedure on the top of the newly-formed layers, which perpendicularly grew into the final morphology. The above results illustrate a new composite film with 1D nanocolumns topologically stacked on the 2D graphene substrate.

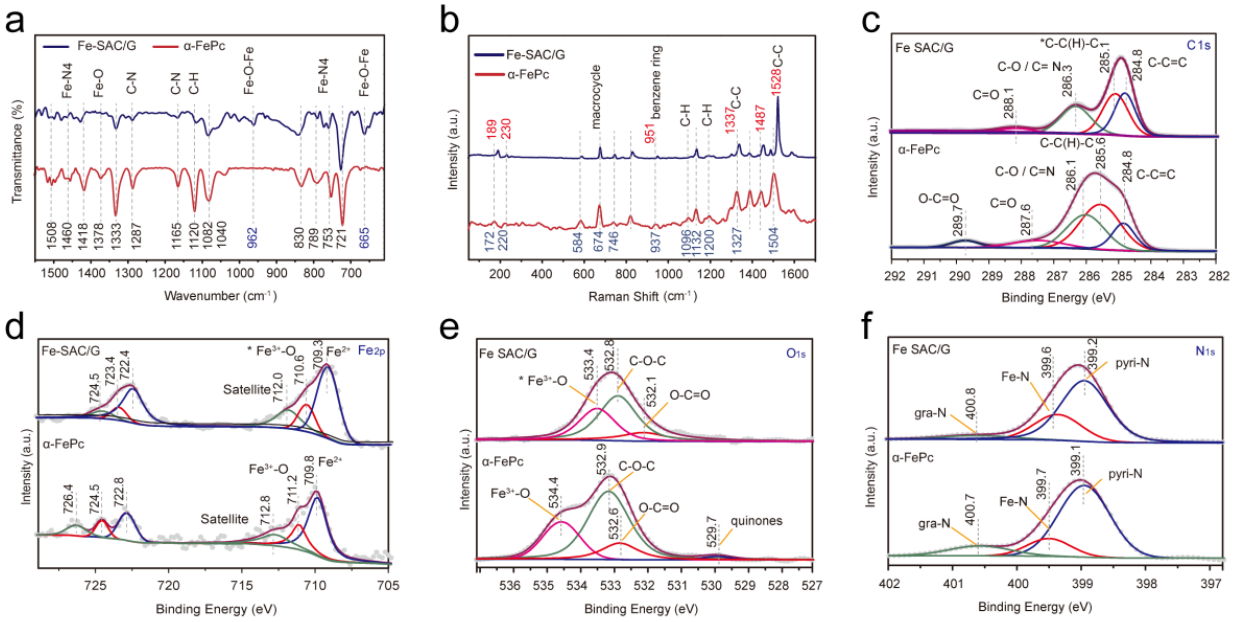

Figure 2. Microstructure and Fe coordination analysis. a) FTIR spectra, b) Raman spectra, c) C_{1s} XPS, d) Fe_{2p} XPS, e) O_{1s} XPS and f) N_{1s} XPS spectra of Fe SAC@G-110 and precursor α-FePc.

2.2 Microstructure and Fe coordination analysis

The FTIR spectrum (Figure 2a) of Fe SAC@G-110 shows the ratio (1:10) of the intensity between peak at 1120cm^{-1} and 721cm^{-1}, representing the vibration of C-H bonds and Fe-N_4 skeleton structure, is much smaller compared with that (1:3) of pristine α-FePc, signifying the removal of partial edge-H atoms from α-FePc during the synthesis process [16]. In addition, the FTIR spectrum of α-FePc shows a peak at 1378 cm^{-1}, representing the stretching vibration of Fe-O bond. The existence of Fe-O component in α-FePc could be attributed to the natural oxygen affinity of active Fe^{2+} ions[17]. It is interesting to find the Fe-O peak at 1378 cm^{-1} vanished while two extra peaks at 665 cm^{-1} and 962 cm^{-1} (stretching and bending vibrations of

Fe-O-Fe bonds, respectively) in the FTIR spectrum of the catalyst, suggesting a new kind of Fe-O coordination configuration[18]. Moreover, the Raman spectrum (Figure 2b) of Fe SAC@G-110 also exhibits the intensity of the C-H vibration peaks at 1096 cm^{-1} and 1200 cm^{-1} decreases compared with that of α-FePc, indicating the removal of H atoms after synthesis[19], which is in agreement with the FTIR results. In addition, the peak of α-FePc at 1504 cm^{-1}, representing the C-C(H)-C stretching vibration, shifted to 1528 cm^{-1} in the Raman spectrum of Fe SAC@G-110[19]. The above Raman shifts signify that the C-C bonding environment in the catalyst was slightly altered, which probably caused by the degeneration of hydrogen. Furthermore, the Raman peak of α-FePc at 172 cm^{-1}, 220 cm^{-1} and 674 cm^{-1}, representing the stretching vibrations of the Fe-N_4 marcocycles[19], shifts to 189 cm^{-1}, 232 cm^{-1} and 676 cm^{-1}, respectively, in the Raman spectrum of Fe SAC@G-110, which could be assigned to the coordination environment variation of Fe center that caused by the altered Fe-O connections. The above results illustrate that the Fe-N_4 planar coordination was retained while the corresponding macrocyclic configuration underwent some variations during the synthesis.

The C_{1s} XPS spectrum of α-FePc (Figure 2c) shows five main peaks at 284.8 eV, 285.6 eV, 286.1 eV, 287.6 eV and 289.7 eV, which can be assigned to C-C=C, C-C(H)-C, C-N/C-O, C=O and O-C=O component, respectively[20]. For Fe SAC@G-110, the binding energy of C-C(H)-C component shifts to 285.1 eV (denoted as *C-C(H)-C) and the relative ratio between C-C(H)-C and C-C=C components decreases from 2:1 to 1:1 compared with that of precursor α-FePc, probably resulting from the mutual C-C bonds spontaneously formed between the edge-C atoms of the H-tailored intermediates. Moreover, the Fe_{2p} XPS spectrum of Fe SAC@G-110 (Figure 2d) shows no peak near 707eV (representing the Fe^0 component), further demonstrate the complete-maintaining of Fe-N_4 macrocyclic structures without any Fe aggregation. The $Fe_{2p2/3}$ XPS spectrum of the pristine α-FePc (Figure 2d) manifests two main peaks at 709.8eV and 711.2eV, which can be assigned to Fe^{2+} and Fe^{3+}-O component, respectively. The binding energy of Fe^{3+}-O component shifts negatively to 710.6eV in the $Fe_{2p2/3}$ XPS spectrum of Fe SAC@G-110, indicating that Fe^{3+} ions in the Fe^{3+}-O component tend to obtain electrons during the formation of the catalyst. Of note, the electron transfer can be attributed to the coordination variation in the FeN_4-O configuration that in consistent with the Raman results. The O_{1s} XPS spectra (Figure 2e) shows the binding energy of Fe^{3+}-O

component of Fe SAC@G-110 obviously shifts negatively (denoted as *Fe^{3+}-O) compared with α-FePc, whereas no such evidence is observed between the binding energy of Fe-N component in the N_{1s} XPS spectra of α-FePc and the catalyst (Figure 2f). This illustrates the coordination variation in Fe SAC@G-110 exactly existing between Fe and O while the Fe-N coordination nearly remaining unaltered, in consistence with the FTIR and Raman results. The above results suggest the selective removal of the edge-H atoms in α-FePc molecules while the maintenance of Fe-N_4 macrocyclic structures, which results in the spontaneous recombination of the generated atomic-Fe structures during the synthesis. In addition, the oxygen in α-FePc (Fe^{3+}-O), introduced by the natural oxidation of active Fe^{2+} ions, was also partially reserved and inserted in the Fe-N coordination during the preparation, which exerts significant influence on the electronic structure of Fe center.

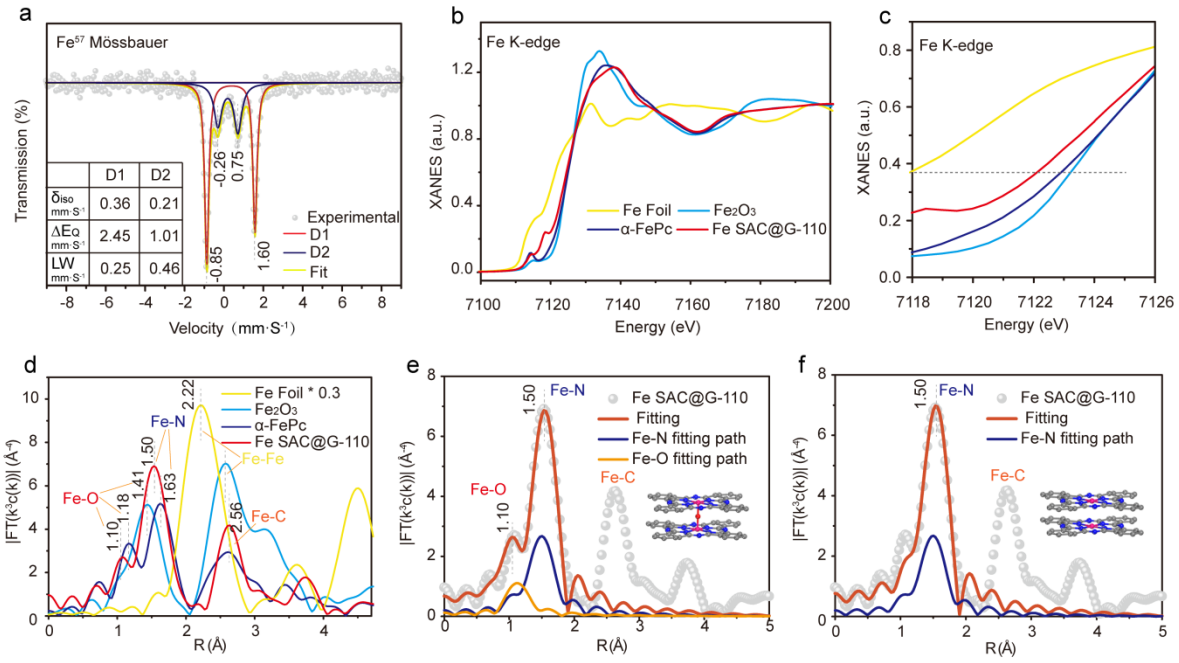

Figure 3. Fe fine structure analysis. a) ^{57}Fe Mössbauer spectrum of Fe SAC@G-110. b, c) Fe K-edge XANES spectra, d) k^3-weighted χ(k) function of the EXAFS spectra of Fe SAC@G-110, precursor α-FePc, Fe foil and Fe_2O_3. EXAFS fitting curves based on the theoretical models e) with and f) without an intercalated O atom between a pair of opposite Fe-N_4 structures.

2.3 Fe fine structure analysis

The ^{57}Fe Mössbauer spectrum (Figure 3a) of Fe SAC@G-110 was fitted with two asymmetrical doublets, D1 and D2, with intensity ratio of nearly 0.65: 0.35. D1, which exhibits

relatively large values of isomer shift (δ_{iso}) of 0.36 and quadrupole splitting (ΔE_Q) of 2.45, can be assigned to the square-planar Fe^{2+}-N_4 coordination with Fe^{2+} in high spin state[21]. Moreover, D1 shows a peculiar line width of only 0.24, which is much smaller compared with recently reported Fe-N_4 SACs, due to the highly-organized Fe coordination structure formed during the growth procedure. D2, with a relatively smaller δ_{iso} value of 0.21 and a ΔE_Q value of 1.01, can be assigned to the pyramid-type $Fe^{3+}N_4$-O coordination with Fe^{3+} in low spin state[21b]. X-ray absorption near-edge structure (XANES) spectra (Figure 3b, c) show that the white-line intensity of Fe SAC@G-110 positions between that of Fe foil and α-FePc, demonstrating the Fe ions tended to obtain electrons when α-FePc molecules lost edge-H atoms and self-assembled with each other, in line with the XPS analysis. As for the R-space of the extended X-ray absorption fine structure (EXAFS), the pristine α-FePc shows two main peaks at 1.18 Å and 1.63 Å (Figure 3d), which can be assigned to Fe-O and Fe-N bonds, respectively, according to the corresponding fitting results (Figure S9 and Table S2, Supporting Information). The Fe-N peak of α-FePc positions higher than that of the normal square-planar Fe-N_4 coordination (1.49 Å)[22], which can be attributed to the stronger electronegativity of O than N atom that pulls the Fe atoms out of the in-plane Fe-N_4 sites. In addition, compared with the EXAFS spectrum of α-FePc, the Fe-O peak of Fe SAC@G-110 slightly shifts to 1.10 Å and the Fe-N peak shifts back to 1.50 Å. The shrinking of Fe-O bonds and extending of Fe-N bonds in Fe SAC@G-110 compared with precursor α-FePc could be attributed to configurational variations in Fe-O coordination that weaken the interaction strength between Fe and O atoms. In order to confirm the Fe coordination structure, the R-space EXAFS spectrum of the catalyst was fitted based on two theoretical models (Figure 3e, f), Fe-N_4 coordination and a pair of opposite Fe-N_4 coordination with an intercalated O atom (FeN_4-O-FeN_4 bridge site) with Fe-O-Fe bonds, respectively. The corresponding fitting results of the two models (Table S2, supporting information) shows that the FeN_4-O-FeN_4 bridge site with relatively smaller R factor of 0.002 is the optimal fitting situation to explain the EXAFS results. The coordination number of Fe-N bond calculated from the fitting results is 4.0 and the bonding length is 1.94 Å, slightly shorter than that (1.98 Å) of α-FePc. Besides, the calculated coordination number and bonding length of Fe-O bond is 0.3 and 1.66 Å, indicating the FeN_4-O-FeN_4 bridge site with an interlayer spacing of 3.32 Å occupies nearly 30% of the Fe coordination structure, in line with the XRD

and Mössbauer analyses. The aforemetioned results suggest the FeN_4-O sites (Fe^{3+}-N_4 sites with axial Fe-O coordination) in α-FePc were partially reserved during the synthesis and the axial O atoms were intercalated into a pair of opposite Fe^{3+}-N_4 sites to form the FeN_4-O-FeN_4 bridge structure in Fe SAC@G-110. During this procedure, the Fe^{3+} ions tended to obtain electrons and the interlayer spacing between the pristine Fe-N_4 coordination were slightly amplified from 3.19Å to 3.32Å to yield staggered-layer configurations, which is in consist with the HR-TEM results.

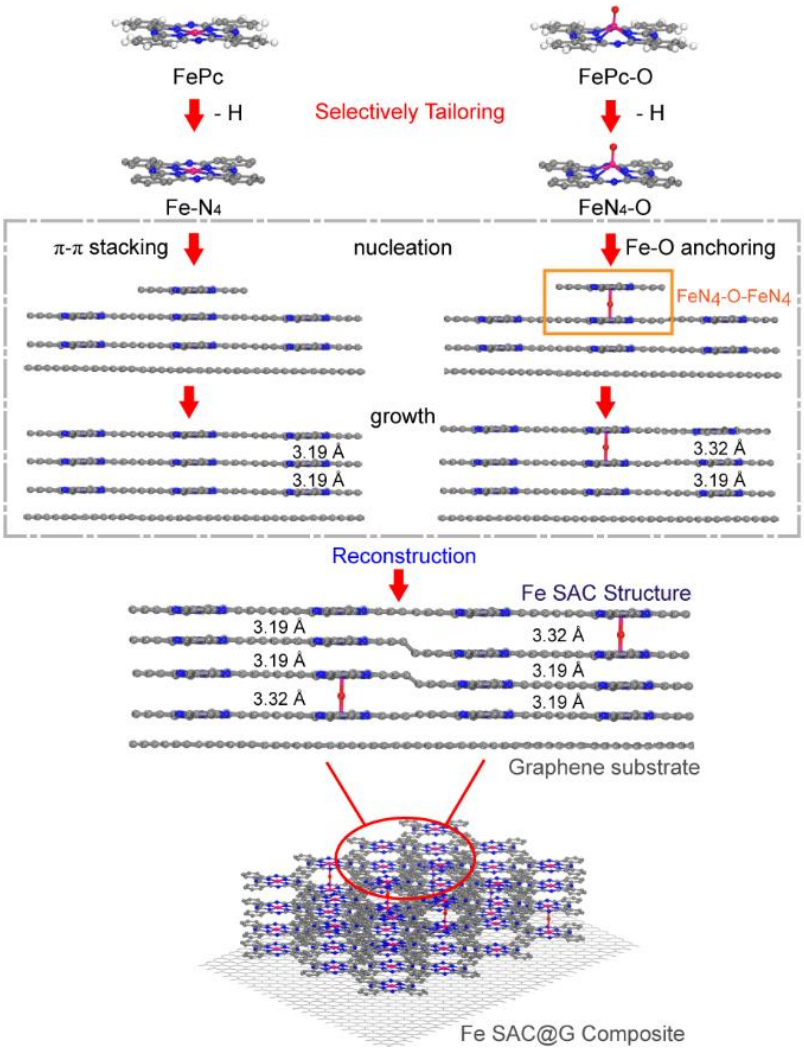

Figure 4. Schematic mechanical illustrations for the formation of 1D nanocolumns conjugated 2D graphene in Fe SAC@G-110 composite film through reconstruction procedure after selectively tailoring α-FePc molecules.

2.4 Potential formation mechanism proposed for Fe SAC@G-110

To further illustrate the structural alteration of Fe-N_4 in α-FePc during the synthesis of Fe SAC@G-110, a potential formation mechanism (Figure 4) is proposed based on the forementioned results, which is briefly described here: 1) Tailoring procedure: Precursor α-FePc molecules, containing two types of Fe components (Fe^{2+}-N_4 and $Fe^{3+}N_4$-O), firstly underwent edge-H tailoring off, meanwhile the Fe-N_4 macrocycles and partial FeN_4-O coordination were reserved during the thermal treatment. As a result, two types of Fe intermediates with or without an axial O coordinate (FeN_4-O and Fe-N_4, respectively) were formed. 2) Reconstructing procedure: The above chain-free intermediates were transferred to the low-temperature region by nitrogen, nucleated and self-assembled on graphene substrate. During this procedure, the nucleation of Fe-N_4 sites, due to the π-π stacking effect of Fe-N_4 macrocycles, would lead to the growth of Fe SAC layers with interlayer spacing of 3.19 Å. For FeN_4-O, the O atoms tended to spontaneously anchor on Fe centers from the body structure to form a new kind of Fe coordination, single O atom intercalated between two opposite Fe atoms (FeN_4-O-FeN_4), which would lead to the extensive interlayer spacing of 3.32 Å. Finally, the staggered layer-like 1D nanocolumns, containing two kinds of Fe nanostructures (FeN_4-FeN_4 and FeN_4-O-FeN_4) with different interlayer spacing (3.19 Å and 3.32 Å, respectively) were formed and grew like a forest.

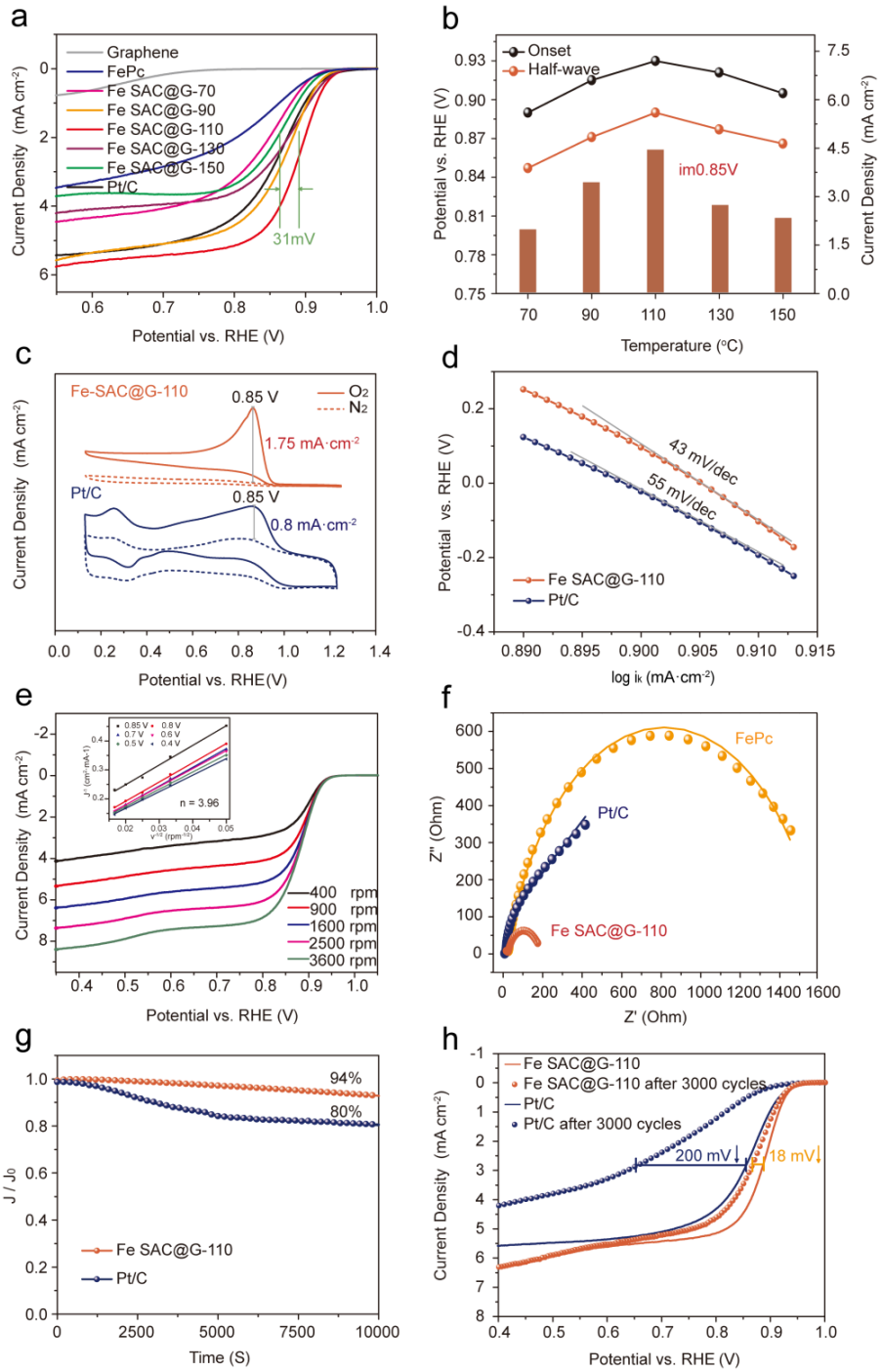

Figure 5. ORR performance of Fe SAC@G. a) LSV curves, b) the corresponding onset potentials (E_{onset}), half-wave potentials ($E_{1/2}$) and current density at 0.85 V (i_m0.85V) of Fe SAC@G synthesized under different growth temperature. c) CV curves. d) Tafel plots. e) RDE LSV curves at different rotating speeds, inside e) is the corresponding K-L plots. f) EIS curves of Fe SAC@G-110, α-FePc and Pt/C catalyst. g) i-t curves for 10000 s and h) LSV curves before and after accelerated durability testing for 3000 cycles of Fe SAC@G-110 and Pt/C. All measurements were conducted in 0.1 M KOH solution saturated with O_2.

2.5 ORR performance

The influence of synthesis temperature of the Fe SAC@G on the ORR performance was evaluated by linear sweep voltammetry (LSV) in 0.1 M KOH solution using commercial Pt/C catalyst as the benchmark (Figure 5a). The LSV curves of all measured Fe catalysts show higher steady-state current than that of pure graphene and α-FePc. Figure 5b shows that with the synthesis temperature ascending from 70 to 110 ^{o}C, the onset potential (E_{onset}), half-wave potential ($E_{1/2}$) and ORR current at 0.85 V (i_m0.85V) of the catalysts increase, which can be attributed to the improving crystalline property and formation of the FeN_4-O-FeN_4 bridge sites under the condition of higher growing temperature based on SEM, XRD and Raman results (Figure S10, S11 and S12, Supporting Information). However, for the catalysts with higher growth temperature (>110 ^{o}C), the ORR efficiency quickly descended, probably due to the shrink of specific surface area (Figure S10) and the collapse of the FeN_4-O-FeN_4 bridge sites. The optimal Fe SAC@G-110 exhibited an E_{onset} of 0.93V, an $E_{1/2}$ of 0.89 V and an i_m0.85V of 3.90 mA·cm^{-2}, much larger than that of Pt/C catalyst (0.92 V, 0.85 V and 3.05 mA·cm^{-2}, respectively). The current density of the ORR peak near 0.85 V vs. RHE in the CV curve (Figure 5c) of Fe SAC@G-110 is 1.75 mA·cm^{-2}, much larger than that of Pt/C (1.30 mA·cm^{-2}). Besides, Tafel slope (Figure 5d) of Fe SAC@G-110 is 43 mV/decade, which is smaller compared with that of Pt/C (55 mV/dec), suggesting a better ORR kinetic efficiency. Moreover, according to the LSV curves based on different RDE rotating speeds (Figure 5e) and the corresponding Koutecky-Levich (K-L) plots, the electron transfer number (n) calculated from the slopes is about 3.96 at the potential range from 0.4 to 0.85 V, indicating a direct 4-electron transfer pathway taking place on the surface of Fe SAC@G-110. Furthermore, according to the electrochemical impedance spectroscopy (EIS) plots (Figure 5f) and the corresponding equivalent circuit model (ECM) (Table S3, Supporting Information), Pt/C catalyst includes an extra component of Warburg impedance (W), representing the mass-transfer effect, compared with Fe SAC@G-110, indicating a higher mass-transfer efficiency of dissolved O_2 between the electrolyte and solid surface[23]. In addition, the charge transfer resistance (R_{ct}) of Fe SAC@G-110 (159.9 Ω) is much smaller than that of Pt/C (269.6 Ω) and α-FePc (1540.7Ω), suggesting the superior Faraday kinetics of the new catalyst. Furthermore, the stability testing results (Figure 5g) shows only 6% of decay occurred in the i_m0.85 for Fe SAC@G-110 after testing

for 10000s while Pt/C showed 20% decay, manifesting the excellent ORR durability of Fe SAC@G-110. Moreover, the accelerated durability testing results (Figure 5h) also exhibit a much better operating stability of Fe SAC@G-110 after testing for 3000 cycles compared with Pt/C, implying the operation robustness of the catalyst.

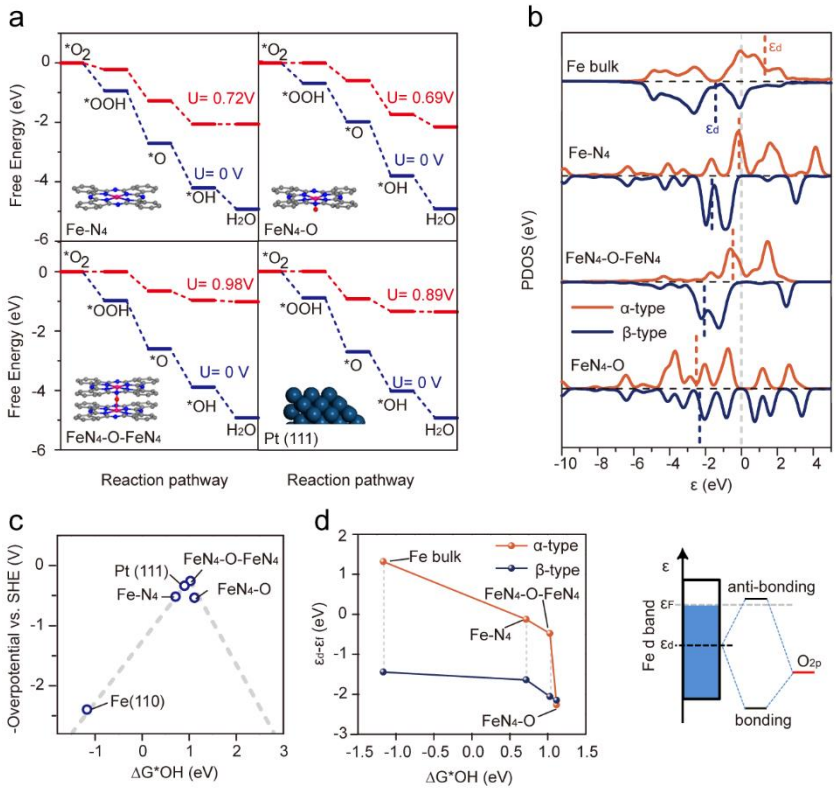

Figure 6. DFT-D computational analysis. a) Free energy diagrams for Fe-N_4, FeN_4-O, FeN_4-O-FeN_4 and Pt (111) sites, insides are the corresponding theoretical models. b) PDOS plots and c) activity volcano plots calculated for Fe bulk, Fe-N_4, FeN_4-O and FeN_4-O-FeN_4 structures. d) Relationship plot between the d band center (ε_d) and ΔG_{*OH} for each model. e) Schematic illustrations for the bonding mechanism between Fe d band and O_{2p} orbital.

2.6 Origin for outstanding ORR performance

Despite the improving crystalline properties and structure stability for catalysts synthesized in higher temperature, the intrinsic reactive capacity of individual active sites is equivalently crucial to the ORR performance. To further study the origin for the superior activity and potential ORR mechanism for Fe SAC@G-110, high-precision DFT-D calculations based on five theoretical models (bulk Fe (110), pristine Fe-N_4, FeN_4-O, bridge FeN_4-O-FeN_4 and Pt (111)) were performed and the results are shown in Figure 6. A uniform 4-electron associate

mechanism with four kinds of intermediates (*O_2, *OOH, *O and *OH) was assumed to simulate the ORR procedure within the selected models and evaluate the corresponding catalytic activities (Table S4, Supporting Information)[24]. The free energy diagrams (Figure 6a, Table S5 and S6, Supporting Information) manifest the rate of ORR process at the FeN_4-O-FeN_4 bridge site is determined by the reduction and desorption step of *OH. Besides, the FeN_4-O-FeN_4 site exhibits the highest applied potential (0.98V vs. SHE) among the theoretical models, much higher than that of Pt (111) (0.89V vs. SHE). The negative over-potential ($-\eta_{SHE}$) vs. ΔG_{*OH} plot (Figure 6c) shows the Pt-comparable ORR performance of FeN_4-O-FeN_4 sites, at the apex of the volcano plot, probably originating from its mild interaction with ORR intermediates[25]. Besides, the Fe-N_4 and Fe-N_4-O sites tend to bind with *OH too strongly or too weakly, resulting in their non-ideal ORR performance [26]. Furthermore, the partial density of states (PDOS) calculated for each model exhibits that the d band centers (ε_d) (both α-type and β-type electrons) of Fe-N_4 shift to lower energy level when coordinated with axial O atoms (Figure 6b and 6d, Table S7, Supporting Information). The smaller value of ε_d in Fe d band could decrease the energy level of anti-bonding orbital between Fe and O atoms, which could be filled with a larger number of electrons to weaken the Fe-O bonding orbital (Figure 6e). Particularly, the ε_d of FeN_4-O-FeN_4 site positions between that of FeN_4 and FeN_4-O sites, resulting in the optimum bonding strength between Fe and O atoms and thus the ideal ORR activity comparable to Pt (111).

3 Conclusion

In summary, a low-temperature strategy was described for synthesis of a self-supporting catalytic composite film through selectively tailoring α-FePc to reconstruct 1D atomic-Fe nanocolumns on large-scale 2D monolayer graphene (Fe SAC@G). The final product exhibited staggered-stratiform structure composed by two types of Fe coordination configurations (Fe^{2+}-N_4 site and $Fe^{3+}N_4$-O-$Fe^{3+}N_4$ bridge site). Compared with the commercial Pt/C catalyst, the new catalyst synthesized at a growth temperature of 110 ^oC (Fe SAC@G-110) exhibited superior ORR activity and operating durability, due to 1) enhanced electron conductivity and structural stability originating from the compact interaction between Fe coordination and graphene substrate; 2) higher intrinsic activity of FeN_4-O-FeN_4 structure compared with primary Fe-N_4 structures. These findings shed light on novel synthesis of ORR catalyst by transforming the

traditional forms of nanostructures from 0D/1D into 0D/1D coupled 2D composite styles through economical pathways, which will show significant potentials for the mass application of energy conversion devices.

Experimental Section

Synthesis of G/Cu: 1cm ×1cm sized copper foil (30μm in thickness) was first annealed at 1050℃ for 1.5h in the atmosphere of Ar and H_2. Next, the heating tempature was adjusted to 1000℃, followed by injecting a mixture flow (CH_4: H_2= 12: 48 sccm) and keeping for 30min to grow graphene film on the copper foil. Upon completing growth, the G/Cu films were rapidly cooled down to room temperature.

Synthesis of Fe SAC@G: Two connected and sealed chambers were heated at T1 (450 ^oC) and T_2 (70 ^oC ~150 ^oC), respectively, in inert atmosphere. The fluffy α-FePc powder (50 mg) was loaded in the first chamber (T_1), thermal treated for 1h, and the G/Cu substrate was loaded in the second chamber (T_2). Next, 200 sccm Ar was flowed in to transfer the sublimated species to the second chamber (T_2) within 1.3 torr Ar atmosphere and kept for 30min. The obtained sample was floated in 0.1 M $FeCl_3$ for more than 12h to etch away the copper layer. The final sample was denoted as Fe SAC@G. More details are presented in the Supporting Information.

Electrochemical Measurements for ORR: All the measurements were conducted in a conventional 3-electrode system: The catalyst film supported on a glassy carbon electrode (GCE) with a diameter of 5mm was served as the working electrode; a ruthenium-titanium mesh and a Hg/HgO (1 M KOH) electrode were used as the counter electrode and the reference electrode, respectively. All the electrode potentials in this work were converted to the reversible hydrogen electrode (RHE) without further description. Datails for fabrication of the electrodes and electrocatalytic tests are presented in the Supporting Information.

DFT-D Computational methods: Spin-unrestricted DFT calculations were performed with the Dmol^3 code. The generalized gradient approximation of Perdew-Burke-Ernzerhof (GGA-PBE) was employed as an exchange-correlation function. The double numerical plus polarization (DNP) was selected and a 4.8 Å orbital cut off was applied as the basis set through all calculations. Datails for DFT-D computational methodologies and models are presented in the Supporting Information.

Acknowledgements

This work was financial supported by the Key Laboratory of Metal Fuel Cell of Sichuan Province, China. The DFT simulations are conducted based on the high-quality computational services provided by Tianjin University.

Reference

[1] C. Lin, X. Li, S. S. Shinde, D. H. Kim, X. Song, H. Zhang, J. H. Lee, *ACS Appl. Energy Mater.* **2019**, *2*, 1747-1755.

[2] A. A. Gewirth, M. S. Thorum, *Inorg. Chem.* **2010**, *49*, 3557-3566.

[3] a) M. Shao, Q. Chang, J. P. Dodelet, R. Chenitz, *Chem. Rev.* **2016**, *116*, 3594-3657; b) J. Masa, W. Xia, M. Muhler, W. Schuhmann, *Angew. Chem. Int. Ed.* **2015**, *54*, 10102-10120; c) X. Zhou, J. Qiao, L. Yang, J. Zhang, *Adv. Energy Mater.* **2014**, *4*, 1301523.

[4] a) J. Gu, C. S. Hsu, L. Bai, H. M. Chen, X. Hu, *Science* **2019**, *364*, 1091-1094; b) J. Li, S. Chen, N. Yang, M. Deng, S. Ibraheem, J. Deng, J. Li, L. Li, Z. Wei, *Angew. Chem. Int. Ed.* **2019**, 201902109; c) W. J. Jiang, L. Gu, L. Li, Y. Zhang, X. Zhang, L. J. Zhang, J. Q. Wang, J. S. Hu, Z. Wei, L. J. Wan, *J. Am. Chem. Soc.* **2016**, *138*, 3570-3578; d) W. Li, S. Xue, S. Watzele, S. Hou, J. Fichtner, A. L. Semrau, L. Zhou, A. Welle, A. S. Bandarenka, R. A. Fischer, *Angew. Chem. Int. Ed.* **2020**, *59*, 5837-5843

[5] C. X. Zhao, B. Q. Li, J. N. Liu, Q. Zhang, *Angew. Chem. Int. Ed.* 10.1002/anie.20203917

[6] a) Y. Liu, B. Huang, X. Zhang, X. Huang, Z. Xie, *J. Power Sources* **2019**, *412*, 125-133; b) M. Sun, D. Davenport, H. Liu, J. Qu, M. Elimelech, J. Li, *J. Mater. Chem. A* **2018**, *6*, 2527-2539.

[7] J. C. Li, Z. Q. Yang, D. M. Tang, L. Zhang, P. X. Hou, S. Y. Zhao, C. Liu, M. Cheng, G. X. Li, F. Zhang, H. M. Cheng, *NPG Asia Materials* **2018**, *10*, e461.

[8] C. Cheng, S. Li, Y. Xia, L. Ma, C. Nie, C. Roth, A. Thomas, R. Haag, *Adv. Mater.* **2018**, e1802669.

[9] N. Zion, D. A. Cullen, P. Zelenay, L. Elbaz, *Angew. Chem. Int. Ed.* **2020**, *59*, 2483-2489.

[10] Y. Qu, L. Wang, Z. Li, P. Li, Q. Zhang, Y. Lin, F. Zhou, H. Wang, Z. Yang, Y. Hu, M. Zhu, X. Zhao, X. Han, C. Wang, Q. Xu, L. Gu, J. Luo, L. Zheng, Y. Wu, *Adv. Mater.* **2019**, *31*, e1904496.

[11] a) L. Tang, X. Meng, D. Deng, X. Bao, *Adv. Mater.* **2019**, e1901996; b) Y. Liang, Y. Li, H. Wang, J. Zhou, J. Wang, T. Regier, H. Dai, *Nat. Mater.* **2011**, *10*, 780-786; c) I. S. Kwon, I. H. Kwak, J. Y. Kim, H. G. Abbas, T. T. Debela, J. Seo, M. K. Cho, J. P. Ahn, J. Park, H. S. Kang, *Nanoscale* **2019**, *11*, 14266-14275; d) K. Xiao, D. Jiang, R. Amal, D. W. Wang, *Adv. Mater.* **2018**, *30*, e1800400.

[12] S. Yang, Y. Yu, M. Dou, Z. Zhang, L. Dai, F. Wang, *Angew. Chem. Int. Ed.* **2019**, *58*, 14724-14730.

[13] a) A. N. Filippin, V. c. López-Flores, T. C. Rojas, Z. Saghi, V. J. Rico, J. R. Sanchez-Valencia, J. P. Espinós, A. Zitolo, M. Viret, P. A. Midgley, A. Barranco, A. Borras, *Chemistry of Materials* **2018**, *30*, 879-887; b) R. A. Laudise, C. Kloc, P. G. Simpkins, T. Siegrist, *Journal of Crystal Growth*, **1998**, *187*, 449-454.

[14] a) G. Zhu, F. Liu, Y. Wang, Z. Wei, W. Wang, *Phy. Chem. Chem. Phy.* **2019**, *21*, 12826-12836; b) F. Liu, G. Zhu, D. Yang, D. Jia, F. Jin, W. Wang, *RSC Adv.* **2019**, *9*, 22656-22667.

[15] a) K. Yang, L. Liu, L. Zhang, W. Xiao, X. Fei, H. Chen, S. Du, K. H. Ernst, H. J. Gao, *ACS Nano* **2014**, *8*, 2246-2251; b) J. A. Labinger, J. E. Bercaw, *Nature*, **2002**, *417*, 507-514.

[16] a) Q. Wang, H. Li, J. H. Yang, Q. Sun, Q. Li, J. Yang, *Appl. Catal. B: Enviro.* **2016**, *192*, 182-192; b) J. Guo, X. Yan, Q. Liu, Q. Li, X. Xu, L. Kang, Z. Cao, G. Chai, J. Chen, Y. Wang, J. Yao, *Nano Energy* **2018**, *46*, 347-355.

[17] K. Chen, K. Liu, P. An, H. Li, Y. Lin, J. Hu, C. Jia, J. Fu, H. Li, H. Liu, Z. Lin, W. Li, J. Li, Y. R. Lu, T. S. Chan, N. Zhang, M. Liu, *Nat. Commun.* **2020**, *11*, 4173.

[18] A. H. Haghighaty, S. M. Dehaghi, *Oriental Journal of Chemistry* **2018**, *34*, 1046-1054.

[19] Z. Liu, X. Zhang, Y. Zhang, J. Jiang, *Spectrochim. Acta. A Mol. Biomol. Spectrosc.* **2007**, *67*, 1232-1246.

[20] T. Taniguchi, H. Tateishi, S. Miyamoto, K. Hatakeyama, C. Ogata, A. Funatsu, S. Hayami, Y. Makinose, N. Matsushita, M. Koinuma, Y. Matsumoto, *Particle & Particle Systems Characterization* **2013**, *30*, 1063-1070.

[21] a) W. Liu, L. Zhang, X. Liu, X. Liu, X. Yang, S. Miao, W. Wang, A. Wang, T. Zhang, *J. Am. Chem. Soc.* **2017**, *139*, 10790-10798; b) U. I. Kramm, L. Ni, S. Wagner, *Adv. Mater.* **2019**, *31*, e1805623; c) A. Zitolo, V. Goellner, V. Armel, M. T. Sougrati, T. Mineva, L. Stievano, E. Fonda, F. Jaouen, *Nat. Mater.* **2015**, *14*, 937-942.

[22] M. Qiao, Y. Wang, Q. Wang, G. Hu, X. Mamat, S. Zhang, S. Wang, *Angew. Chem. Int. Ed.* **2020**, *59*, 2688-2694.

[23] Y. Chen, Z. Li, Y. Zhu, D. Sun, X. Liu, L. Xu, Y. Tang, *Adv. Mater.* **2019**, *31*, e1806312.

[24] W. Liang, J. Chen, Y. Liu, S. Chen, *ACS Catalysis* **2014**, *4*, 4170-4177.

[25] K. S. Exner, *Angew. Chem. Int. Ed.* **2020**, *59*, 10236-10240.

[26] a) J. H. Zagal, M. T. Koper, *Angew. Chem. Int. Ed.* **2016**, *55*, 14510-14521; b) J. K. Norskov, J. Rossmeisl, A. Logadottir, L. Lindqvist, J. R. Kitchin, T. Bligaard, H. Jonsson, *J. Phys. Chem. B* **2004**, *108*, 17886-17892.

Graphical Abstract

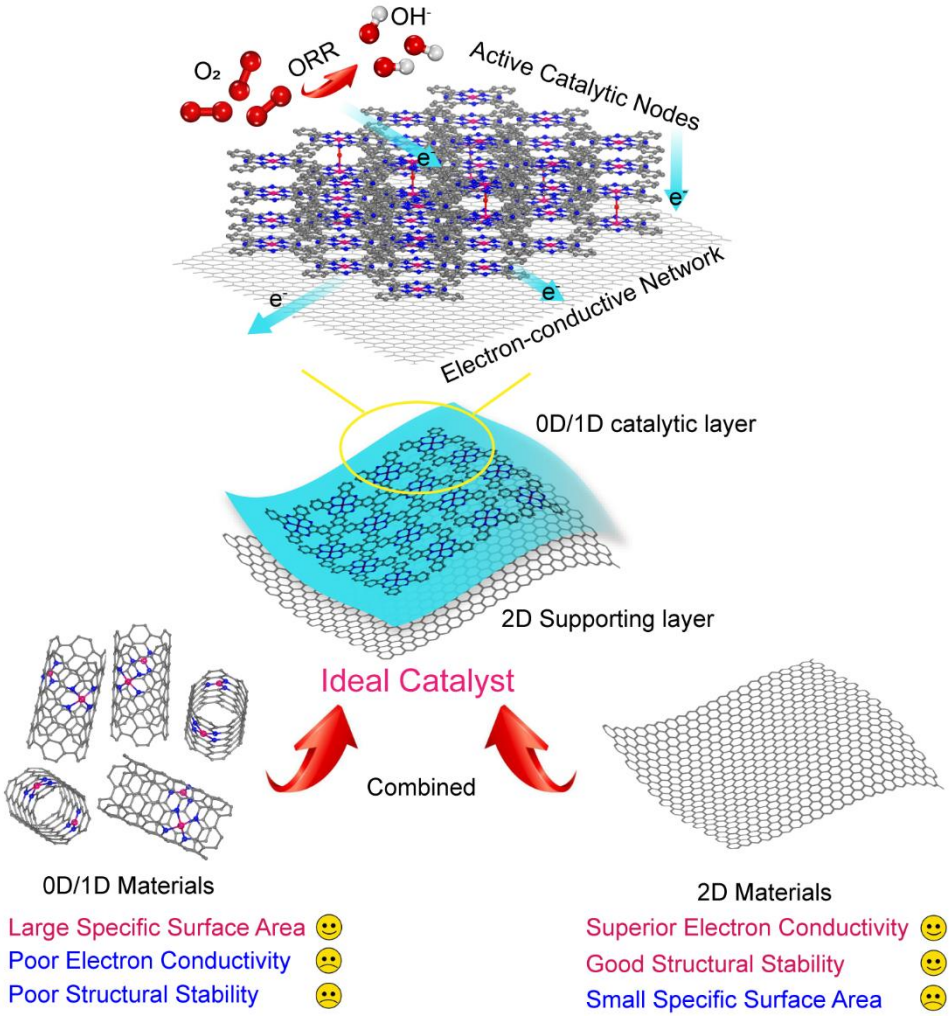

Description: Combination of traditional 0D/1D catalytic structures with electron-conductive 2D networks constructs ideal catalysts for Oxygen Reduction Reaction.

Keywords

Single-atom Catalyst; Oxygen Reduction Reaction; Tailoring; Reconstructing; DFT-D